3 Location procedure

3.1 Event detection

The first step within any location procedure is to find an event within the recorded data stream. For the location method presented in this thesis, this can be accomplished by using an arbitrary automatic P-wave detection algorithm. Several approaches have been proposed for the automatic P-wave arrival detection (e.g., Allen, 1978; Baer and Kradolfer, 1987; Earle and Shearer, 1994; Anant and Dowla, 1997; Bai and Kennett, 2000; Saragiotis et al., 2002; Zhang et al., 2003) using energy analysis, short-term-average and long-term-average (STA/LTA) ratios, statistical analysis, frequency analysis, wavelet analysis, polarization analysis/ particle motion or a combination of those. Which detection algorithm provides the most reliable results often depends on the acquisition geometry and the quality of the data. In this work a detection algorithm that combines STA/LTA ratios, spectrogram analysis and polarization analysis was developed for single three-component receiver detection.

In principle STA/LTA ratios can be described as follows. The STA measures the average amplitude in a short time window and is very sensitive to sudden increases in the amplitude of a time series. In contrast, the LTA measures the average amplitude in a long time window and hence reflects the amplitude of the background noise. For this reason the ratio between the STA and the LTA provides a measure of the signal-to-noise in the considered time window of the STA. In this work three different STA/LTA algorithms proposed by Allen (1978); Baer and Kradolfer (1987) and by Earle and Shearer (1994) were tested. The algorithm proposed by Allen (1978) requires apart from the data also the input of three constants characterizing low-pass filter functions and a threshold. It works very reliable as long as the constants for the low-pass filter functions are assigned carefully. However, the aim of this thesis was to work with very different earthquake data of different dominant frequencies and for this reason this algorithm was not implemented. The algorithms proposed by Baer and Kradolfer (1987) and Earle and Shearer (1994)

do not require the input of constants for the low-pass filter functions which is beneficial for the application to various different types of events. For the data considered in this work both algorithms provided similar reliable results but the latter one was found to be computationally much less expensive. Hence the algorithm from Earle and Shearer (1994) was implemented in the event detection method. Figure 3.1 (a) shows traces of synthetic three-component data which contain random noise as well as the P- and S-wave arrivals . The STA/LTA ratio calculated from these data using an STA window of 10 ms and an eight times larger LTA window are shown in Figure 3.1 (b).

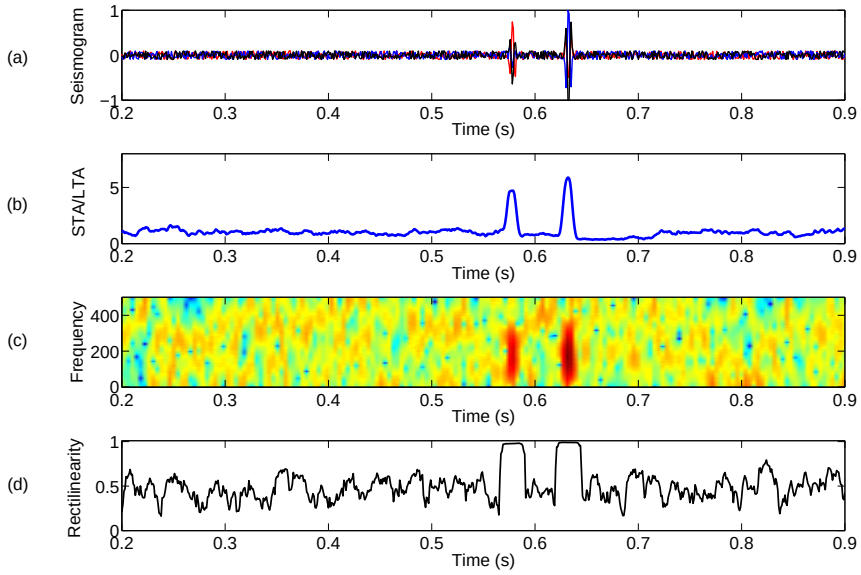

Figure 3.1: Scheme of a detection algorithm that combines STA/LTA ratios, spectrogram analysis and polarization analysis. (a) 3C traces of synthetic data containing noise as well as P-wave and S-wave arrivals, (b) STA/LTA ratio versus time of the data in (a). The length of the STA window was 10 ms and of the LTA window 80 ms. (c) Spectrogram of the data in (a). The intensity in dB is color-coded and increases from cool colors to hot colors. (d) Rectilinearity versus time obtained by equation (2.21) using a moving time window of 20 ms.

A spectrogram analysis is commonly applied for processing of speech signals (Rabiner and Schafer, 1978) and provides information about the time dependent frequency-content in a specified time window of the data. In practice, the frequency spectra of small (overlapping) time windows are computed and displayed as a time series reflecting the intensity of frequencies (Oppenheim and Schafer, 1989). Spectrograms can be utilized for event detection since the arrival of an event changes the frequency-content and the amplitudes compared to the background noise. In Figure 3.1 (c) the spectrogram analysis of the data in Figure 3.1 (a) is shown.

In section 2.3 the principles of polarization analysis are described in detail. This analysis typically yields three parameters. For single receiver detection the rectilinearity is the most meaningful parameter with values close to one for perfectly linearly polarized waves and values close to zero for perfectly spherically polarized waves. Since the rectilinearity allows to distinguish between isotropic background noise, surface waves[1] and body waves it can also be used for event detection at least for signal-to-noise ratios clearly above 1. The rectilinearity time series of the data in Figure 3.1 (a) computed using a moving time window is shown in Figure 3.1 (d).

As shown in Figure 3.1 the STA/LTA ratio, the spectrogram analysis as well as the rectilinearity analysis display sharp onsets in their values at times of the P- and S-wave arrival. These sharp onsets are now used for the event detection. In other words, an event flag is only set if sharp onsets in the time series of STA/LTA ratio, frequency-content and rectilinearity is observed.

This detection algorithm works for single three-component receivers. It is intuitive, that an array of three component receivers provides even more information (e.g., azimuths and dips of the incoming wave) which can be used to increase the robustness of the detection. Later in this thesis array specific observations in the polarization analysis are described and additionally used for event detection as well as for phase identification.

3.2 Location Method

In the presented location method an accurate P-wave onset time is not required. Instead a time interval $[t_1, t_2]$ around the detected P-wave is determined that includes a few cycles of the P-phase arrival. The dominant period of the P-phase arrival is already provided by the spectrogram analysis in the detection algorithm. A relatively small interval length of a few dominant periods of the P-wave will likely exclude the S-phase arrivals. This assumption even holds for typical hydraulic fracture monitoring situations, where the spacing between monitoring and treatment wells results in a clear separation of the body-wave phases. Further, STA/LTA ratios and polarization parameters (especially in array configurations) can be used to exclude other phase arrivals (e.g., reflections) from the selected time interval. This means that the length of the time interval will be automatically shortened when the STA/LTA ratio or the polarization analysis indicates a second arrival. The selected interval and the velocity model are the only input into our location procedure (see Figure 3.2).

The procedure then performs as follows: First the polarization information in the selected time interval is estimated from the three components of the signal. As dis-

[1] Love waves are also characterized by high rectilinearity values (if not disturbed by S-wave coda). On the other hand, Love waves are dispersive which can be recognized in spectrograms.

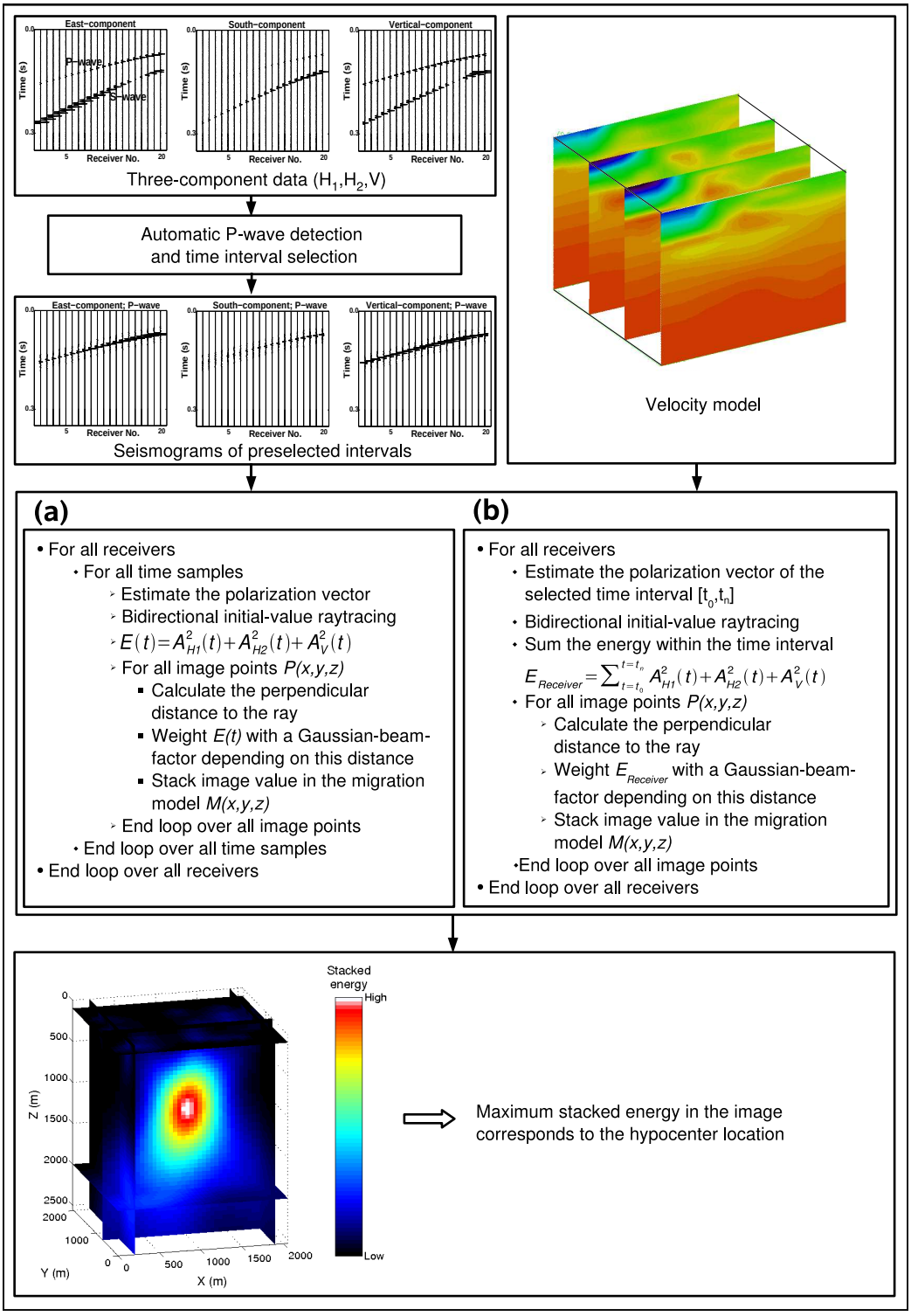

Figure 3.2: Flowchart of the location method: (a) using instantaneous polarization information and (b) using the polarization information of a time interval.

cussed in section 2.3 this can be achieved with a covariance analysis of the whole time window (equations (2.18) - (2.20)) or by considering each time sample separately. The latter provides information about the instantaneous polarization and is the most simple form of polarization analysis. In this work both techniques of polarization estimation were used. Since the location kernel of both techniques does not differ significantly, the location method that uses the instantaneous polarization will be explained first and afterwards the required changes for the use of the covariance-based polarization information will be described.

Location using instantaneous polarization

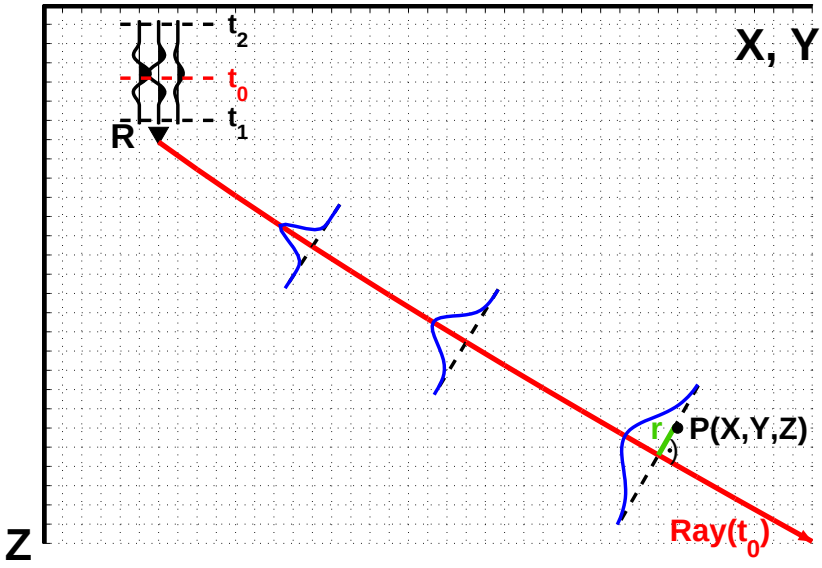

Figure 3.3: Scheme of energy back-propagation. Initial-value ray tracing is performed for the time sample t_0. The perpendicular distance r from a grid point $P(x, y, z)$ to the ray and the corresponding ray length is used for energy weighting. Weight functions for three different ray lengths are shown schematically as blue lines across the ray.

The instantaneous polarization estimated from a single time sample is used as a starting direction for initial-value ray tracing (see section 2.4 and Figure 3.3). This means that every time sample is treated as part of the P-wave arrival. In fact, the instantaneous polarization vector needs to be treated bidirectional because the particle motion can be caused by pressure or tension at the source. In other words, two rays must be traced: one using the instantaneous polarization vector as the starting direction and the second one using the reversed instantaneous polarization vector. However, if the time sample is part of the P-wave then one of the two rays is traced towards the hypocenter (see section 2.3) and if not both rays are traced in random but opposite directions away from the receiver. In any case the ray tracing is performed up to the boundaries of the model. These boundaries are usually

defined by the target of interest, e.g., the volume that is expected to be seismically active. Then a wavefield back-propagation along the whole ray is performed by assigning image values $E(x, y, z, t)$ to every grid point $P(x, y, z)$ of the model (treating both rays individually). These image values are obtained by weighting the energy of the time sample with a Gaussian-beam-type factor (Červený, 2001):

$$E(x, y, z, t) = \left(A_{H1}^2(t) + A_{H2}^2(t) + A_V^2(t)\right) \cdot \exp\left(-\frac{r^2}{b^2}\right). \tag{3.1}$$

A_{H1}, A_{H2} correspond to the amplitudes of the horizontal components and A_V to the vertical component. The weighting is controlled by the perpendicular distance r of the grid point $P(x, y, z)$ from the corresponding ray and the width of the Gaussian beam b. In order to take into account the uncertainty of location with increasing travel path, the raylength $s(P)$ and the dominant wavelength λ_{dom} of the signal are used to control the width b of the Gaussian beam, which is here defined as:

$$b = \sqrt{s(P) \cdot \frac{\lambda_{dom}}{2}}. \tag{3.2}$$

Physically this means that the beam width increases similar to Fresnel zones (Kravtsov and Orlov, 1990; Ishimaru, 1978) with increasing raylength (see Figure 3.3) and increasing wavelength. Significant energy-values are concentrated within the beam width whereas outside the beam width the energy values decrease rapidly. Hence, the weighting restricts the back-propagation along the rays as shown in Figure 3.4. Equation (3.1) leads to a singularity if the beam width obtained from equation (3.2) becomes zero. This problem occurs directly at the receiver locations as well as at all grid points which are perpendicular to the starting direction of the ray at the receiver. In order to avoid such singularities zero values are assigned to these grid points.

Finally, a summation of all image values of the previously selected time interval $[t_1, t_2]$ over all receivers is performed:

$$M(x, y, z) = \sum_{Receiver} \int_{t_1}^{t_2} E_{Receiver}(x, y, z, t) dt. \tag{3.3}$$

The summation over all receivers yields regions of distinct stacked energy. Thus, the region in the final image $M(x, y, z)$ with maximum stacked energy is assumed to represent the hypocenter of the event (see Figure 3.4). Furthermore, it is also possible to correct the energy back-propagation for geometrical spreading. However, this is not a requirement for this location method because in this work the focus is on the kinematically estimated location and not on its dynamic properties. Tests on synthetic data which are presented in the next section will show successful location results for both, migration with and without geometrical spreading correction.

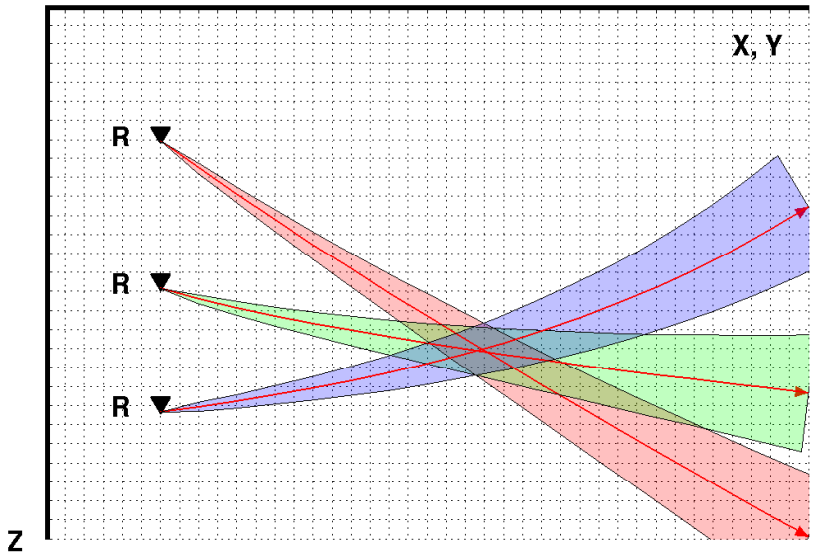

Figure 3.4: Scheme of an image obtained by initial-value ray tracing, energy weighting and summation over three receivers for a time sample t_0. The region with maximum energy is considered to be the hypocenter of the event.

The reliability of the obtained hypocenter can be estimated by calculating the travel times from the hypocenter to each receiver. These travel times can be inverted for time differences between the arrival times at different receivers. At the same time, it is possible to estimate the arrival time differences from the data, for example by using the time differences between the maxima of the STA/LTA ratios in the selected time window or by crosscorrelating the time windows. For a reliable hypocenter the calculated arrival time differences at different receivers have to be consistent with the time differences observed in the data. If this consistency test fails the hypocenter cannot be considered as located.

Location using averaged polarization

The method described above uses instantaneous polarization which is estimated sample by sample in the preselected time interval around the P-wave. As described in section 2.3 it is also possible to estimate one single polarization vector for the preselected time interval. Equation (2.20) yields the eigenvalues $\lambda_1 \geq \lambda_2 \geq \lambda_3$ and eigenvectors p_1, p_2, p_3 that define the polarization ellipsoid that fits the three-component data in the considered time interval. When calculating the polarization ellipsoid for a small time window (that includes a few dominant periods) around the P-wave the eigenvector p_1 with the largest eigenvalue λ_1 represents the propagation vector of the P-wave. Hence the eigenvector p_1 can be used as the starting direction for initial-value raytracing. The eigenvector does not account for the

sign of the first motion which means that we get the same vector by reversing the three-component signal. In this way the obtained eigenvector is also treated as a bidirectional vector, which results in the tracing of two rays with opposite directions from each receiver. Exactly as for the location that uses instantaneous polarization the raytracing is performed to the boundaries of the target of interest. The difference is that using selective raytracing the energy back-propagation needs to be performed cumulatively. This means that the energy of the time interval for each receiver is stacked before the back-propagation:

$$E_{Receiver} = \sum_{t=1}^{N} \left(A_{H1}^2(t) + A_{H2}^2(t) + A_V^2(t) \right) \tag{3.4}$$

where A_{H1}, A_{H2} and A_V are the amplitudes of the three components and N denotes the number of samples in the time interval. Then this energy is propagated backward in space along the two traced rays from each receiver using Gaussian-beam-type weighting factors for each image point as described above:

$$E_{Receiver}(x, y, z) = E_{Receiver} \cdot \exp\left(-\frac{r^2}{b^2} \right). \tag{3.5}$$

When using selective raytracing the time sample dependence of equation (3.3) is removed and only a summation of all image values over all receivers is performed

$$M(x, y, z) = \sum_{Receiver} E_{Receiver}(x, y, z). \tag{3.6}$$

Again, this summation yields regions of distinct stacked energy (see Figure 3.4) and the region with maximum stacked energy is assumed to represent the hypocenter of the event.

Discussion

Event location may require fine volume discretization that can be computationally expensive if a high resolution is expected for large volumes (the size is defined by the target of interest). Tests on reservoir scale (< 1 km^3, e.g., the volume that is expected to be seismically active during hydraulic fracturing) have shown that both location algorithms provide hypocenters within seconds which allows for real time monitoring. Much more challenging is real time event location when regions with natural tectonic activity, like the San Andreas Fault system, are monitored because these regions are usually on the order of several 10 km^3 and much larger than reservoir scale. The location method that uses instantaneous polarization can only provide real time locations for such large volumes when the resolution is decreased. It is intuitive, that tracing only two rays for each time interval instead of two rays for each time sample decreases the computational costs significantly.

Hence, the location method that uses a single polarization vector provides faster location results for larger volumes while preserving the spatial resolution.

It is important to note that averaging the polarization information in a time interval may lead to very smooth results (decrease the resolution) depending on the length of the interval. Especially in the case that the selected time interval accidently contains two interfering arrivals the averaged polarization information combines the dominant polarizations of the two arrivals and leads to a wrong starting direction for the raytracing. As described in section 2.3 instantaneous polarization attributes may resolve the polarization orientation of the uncontaminated part of partly interfering arrivals. On the other hand, the instantaneous polarization attributes may become highly variable depending on the signal-to-noise ratio while the estimate of averaged polarization attributes of a carefully chosen time interval provides more stable results for the same signal-to-noise ratio.

Both methods have their advantages as well as their disadvantages. Depending on the size and the desired resolution the method that averages the polarization information may provide faster results while maybe loosing information when the selected time interval is contaminated with another coherent arrival. The method that uses instantaneous polarization may partly resolve the polarization in contaminated time intervals while loosing the ability of real-time applications for large volumes with fine discretization. Hence the choice of which location method is more robust and efficient depends on the quality of the data as well as on the desired volume discretization and computation time.

3.3 Application to synthetic data

In this section both location methods are applied to synthetic data using different source types and acquisition geometries. Independent of the source type all synthetic data were generated using homogeneous and isotropic models. The different sources were realized using equation (2.11) and the required combinations of the moment tensor. The source-time function was always a Küpper wavelet (Fuchs and Müller, 1971) but the dominant frequency was varied for the different synthetic data.

3.3.1 Explosion source

Synthetic data of an explosion source were modeled with equation (2.13) assigning a constant P-wave velocity of 6000 m/s to a model with dimensions 2000 m x 2000 m x 2500 m. The source was placed at x = 1000 m, y = 700 m and z = 1000 m and a dominant frequency of 40 Hz was used for the source-time function.

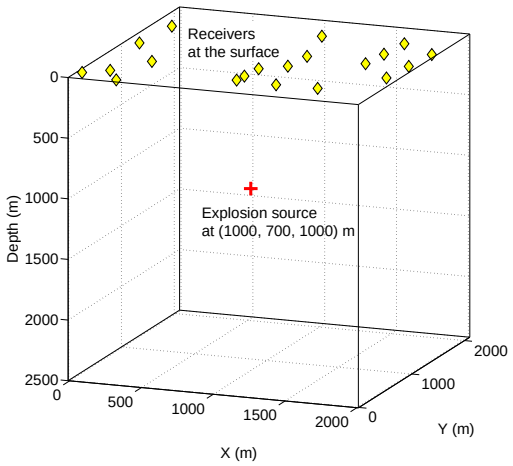

Figure 3.5: Acquisition geometry of the first synthetic data example.

The recording network of the first example consisted of 20 arbitrarily distributed surface stations and is shown in Figure 3.5. Such receiver geometries are sometimes used for surface monitoring of fluid injection experiments as for example for the monitoring of the KTB injection and pumping experiments carried out between 1994 - 2004. (see e.g., Baisch et al., 2002). The three-component data with up to 30 % white noise computed for this model are shown in Figure 3.6. The given percentage of white noise means that the maximum noise amplitudes are restricted to this percentage of the averaged maximum signal amplitude of the 20 receivers.

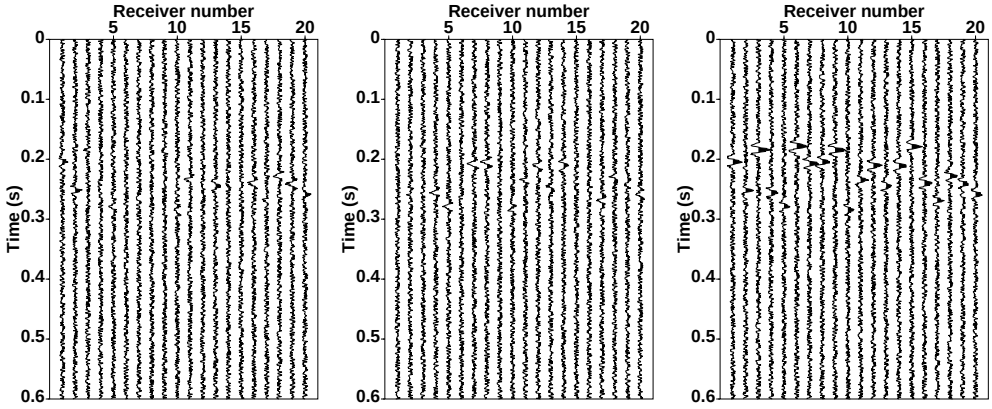

Figure 3.6: Synthetic data radiated from an explosion source and recorded at arbitraily placed three-component surface receivers. From left: x-component, y-component and z-component. All traces contain the P-wave between 0.15 s and 0.3 s.

Since the source of this data set is an exploding point source in an homogeneous isotropic medium the seismograms contain only the P-phase. Knowing that the modeled traces contain neither coherent arrivals of other phases nor any arrivals

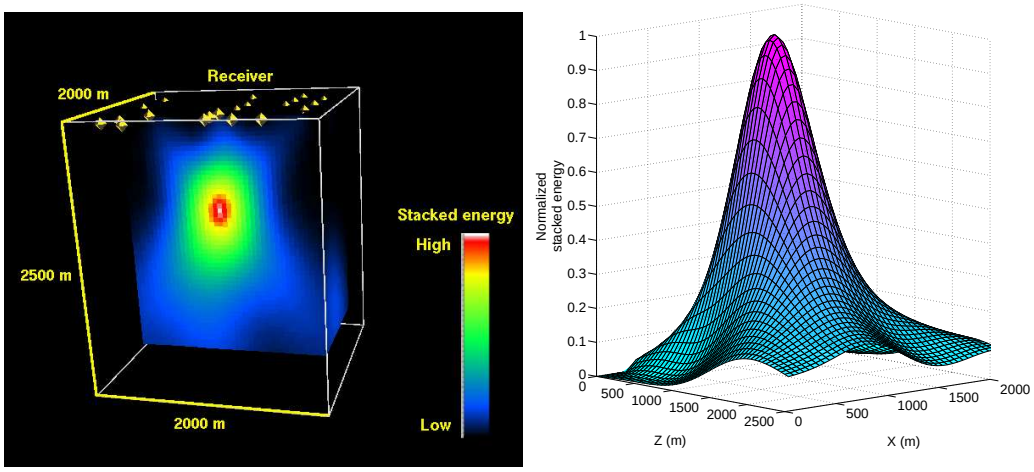

Figure 3.7: Image of the located source. Left: Image slice at y = 700 m. Black and blue colors correspond to small values of stacked energy and red to white colors in the center of this image to large values. The maximum value marks the event location. Right: Distribution of the normalized stacked energy at the left displayed image slice with maximum energy at x = 1000 m and z = 1000 m.

of other events the additional interval selection around the P-phase of each trace was not performed. In orther words, the whole trace was processed. The location method that uses instantaneous polarization (see Flowchart 3.2 (a)) was performed in a migration volume with the dimensions mentioned above and using a grid spacing of 50 m. The imaging result is shown in Figure 3.7 (left) for a slice at y = 700 m. Large image values are visible in the center of the image and mark the location of the hypocenter. In order to get a better impression of this region, the spatial distribution of the normalized stacked energy is shown in more detail in Figure 3.7 (right) for the slice at y = 700 m. Please note that using the whole trace for location propagates more noise energy into the migration model than using a preselected time interval around the P-wave onset. Nevertheless, the stacked energy values within this volume slice decay rapidly away from the maximum. This decay gives a qualitative estimate of the location uncertainty. For this example the coordinates of the maximum energy are observed at the true event coordinates of the model.

For the second example shown here the same exploding point source at x = 1000 m, y = 700 m and z = 1000 m was used. This time, the recording network consisted of a vertically oriented linear array of 20 receivers at a constant spacing of 100 m simulating an array deployed in a borehole at x = 0 m and y = 1500 m (Figure 3.8). Similar recording geometries are commonly used to monitor hydraulic-fracturing operations from monitoring wells (e.g., Urbancic et al., 1999). White noise up to 20 % was added to the three-component data as shown in Figure 3.9. Also, this data set did not contain any other coherent arrivals due to the source type and the model setup. Again the whole trace was used

for location. The location algorithm that uses instantaneous polarization was performed on a migration model with dimensions of 2500 m x 2000 m x 2000 m and a grid spacing of 100 m. Furthermore, a geometrical spreading correction of the backpropagated energy was implemented in the location process.

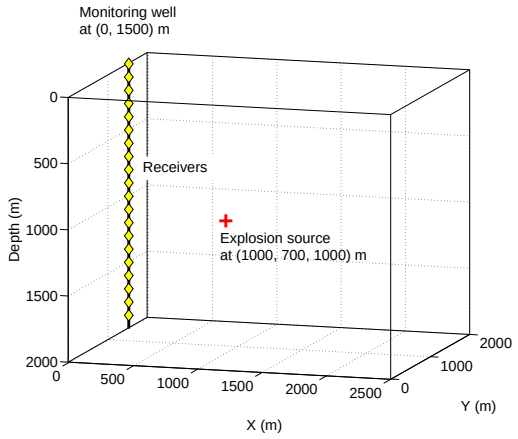

Figure 3.8: Acquisition geometry of the second synthetic data example simulating a monitoring well.

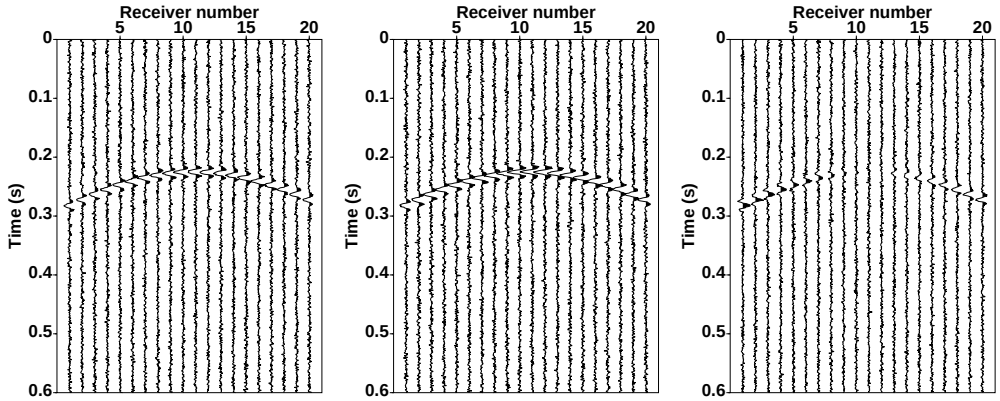

Figure 3.9: Synthetic data radiated from an explosion source and recorded at a vertical array of 20 three-component receivers. From left: x-component, y-component and z-component. All traces contain the P-wave between 0.2 s and 0.3 s.

The resulting image for a slice at z = 1000 m is shown in Figure 3.10 (left). Again, the region of high stacked energy is considered as the event location and the coordinates of the grid point with the maximum energy are the true event coordinates of the source. Due to the receiver geometry all rays which correspond to P-waves from our explosion source were back-propagated at similar azimuths. Thus, the region of high stacked energy shows an elliptical shape with its main extension directed towards the receiver string. The distribution of the normalized stacked

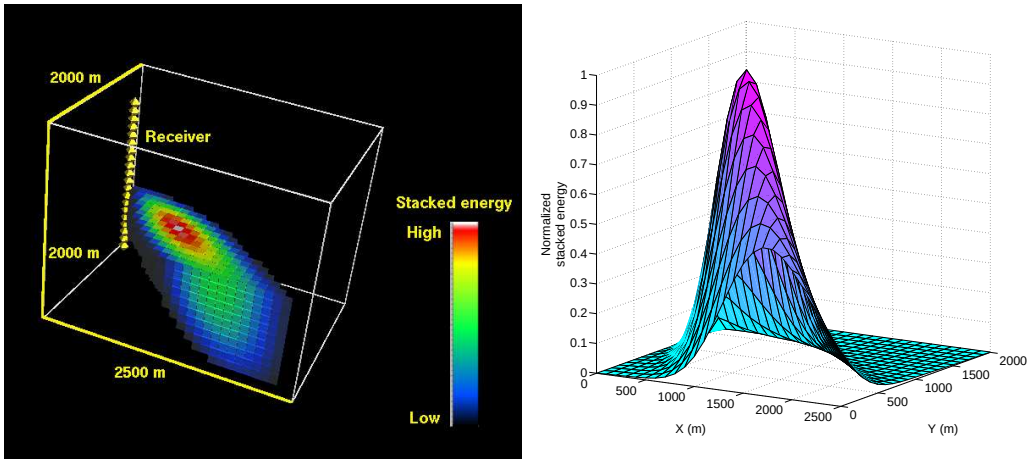

Figure 3.10: Image of the located source. Left: Image slice at z = 1000 m. Colors represent values of stacked energy as described in Figure 3.7. The elliptical region of high stacked energy in the center of this image contains the hypocenter of the event (white spot). Right: Distribution of the normalized stacked energy at the displayed slice of the image above with maximum energy at x = 1000 m, y = 700 m.

energy at slice z = 1000 m as shown in Figure 3.10 (right) also reflects this effect. Also for this example the whole trace was used for location and hence more noise was back-propagated into the migration model. However, the stacked energy also decays rapidly away from the maximum and indicates a good quality for the location. The maximum stacked energy was found at x = 1000 m, y = 700 m and z = 1000 m which corresponds to the synthetic source location. This means the hypocenter of the explosion source was again successfully located. The geometrical spreading correction implemented for energy back-propagation did not influence the location result; only the receiver geometry affected the shape of the likelihood region for the hypocenter.

3.3.2 Double couple source

For the third synthetic data example a double couple source was considered. The source was oriented in the x-z-plane at x = 50 m, y = 100 m and z = 3000 m. A constant P-wave velocity of 5300 m/s and a constant S-wave velocity of 3060 m/s (this corresponds to a Vp-Vs ratio of 1.73) was assigned to a homogeneous isotropic model with dimensions 2000 m x 2000 m x 3500 m. Equations (2.14), (2.15) and (2.16) were used to calculate the particle displacement and the source-time function had a dominant frequency of 180 Hz.

The acquisition geometry consisted of two arrays placed in monitoring wells (#1 at $x = 350$ m, $y = 20$ m and #2 at $x = 250$ m, $y = 350$ m, see Figure 3.11). The first array consisted of 20 receivers with 30 m spacing starting at $z = 2250$ m and the second one of 40 receivers with 15 m spacing starting at $z = 2350$ m.

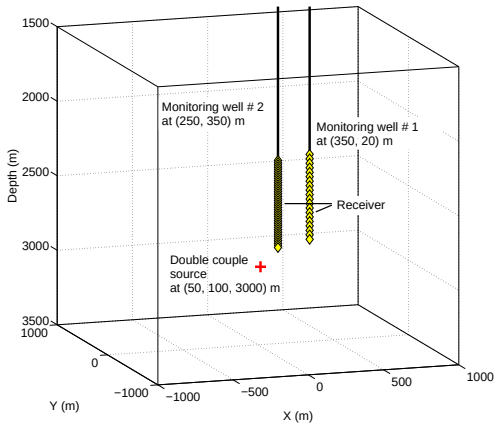

Figure 3.11: Acquisition geometry of the third synthetic data example.

Also this data set was contaminated with 20 % white and isotropic noise. The corresponding seismograms are shown in Figure 3.12.

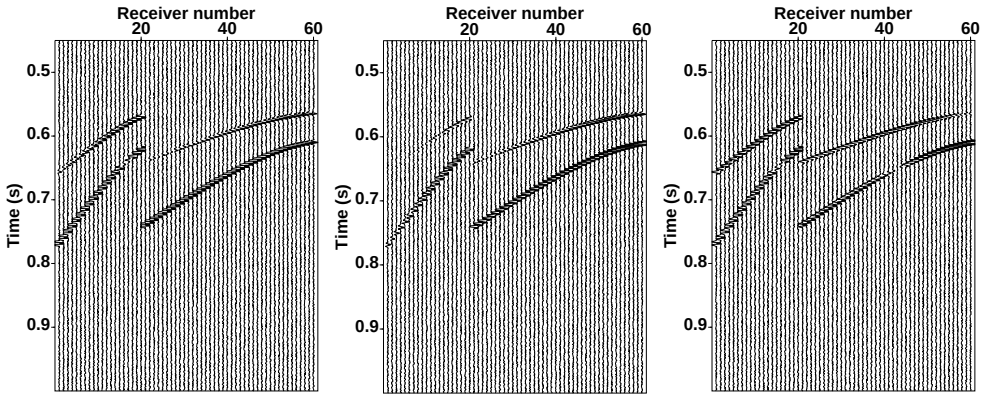

Figure 3.12: Synthetic data set generated with a double couple source in the x-z plane. From left: x-, y- and z-component seismograms with 20 % white noise. The recording system consisted of two vertical arrays (20 receivers in array #1 and 40 in #2).

All traces contain the arrivals of both, P- and S-wave. For this reason it is necessary to select a time interval around the P-wave onset. This means the application of a detection algorithm as well as phase-arrival identification is required. The single receiver detection algorithm described in section 3.1 was applied to this data set. The result obtained for receiver number 18 was already shown in Figure 3.1. If two arrivals are detected at a single receiver it is reasonable to assume that the first detected arrival most likely belongs to the P-wave and the second one to the S-wave. However, as indicated in section 3.1 array configurations can also be utilized for phase-arrival identification. In Figure 3.13 (a) and (b) the single station analysis results for the STA/LTA ratio and the rectilinearity are plotted in time versus receiver number. The single receiver detection algorithm assigned pick flags

to both P- and S-waves at all receivers. In order to distinguish between the P- and the S-wave the fact that the recording network consisted of two vertical arrays can be used. As explained in section 2.3 the azimuth of a P-wave observed on a vertical array will be the same for each receiver in this array (at least in homogeneous isotropic media) unless the receiver array is placed on a nodal plane of the radiated P-wave. In contrast, as demonstrated in section 2.3 the S-wave observed on a vertical array will only show the same azimuth at each receiver in the array when the array is placed on a nodal plane of the radiated SV-wave. For this reason the estimated polarization information (already calculated to obtain the rectilinearity values) were converted into azimuth values using equation (2.23) as shown in Figure 3.13 (c). A test of the azimuth consistency at all receivers placed in the same borehole was performed for the arrivals detected with the single receiver method. The result is shown in Figure 3.13 (d), where each arrival with consistent azimuth values at all receivers in the same borehole is marked with a blue star and an arrival with inconsistent azimuth values with a red star, respectively. The arrival that passed the azimuth-consistency test was assumed to be the P-wave. Using the phase indentification shown in Figure 3.13 (d) the interval around the detected P-wave was selected. From the single receiver spectrogram analysis (see Figure 3.1 (c)) the dominant frequency was estimated as 180 Hz and consequently the dominant period as 0.006 s. For this reason the length of the selected interval around the detected P-wave was chosen to be 0.018 s (three times the dominant period).

Then the selected time intervals were processed with the location method that averages the polarization information for the time interval at each receiver (see Figure 3.2 (b)). The migration model with 25 m regular gridspacing was assigned to the target of interest with x = (-1000, 1000) m, y = (-1000, 1000) m and z = (2000, 3500) m. The maximum stacked energy was found at x = 50 m, y = 100 m and z = 3000 m. The obtained source image is shown in Figure 3.14 (left) at a vertical slice through y = 100 m and in Figure 3.14 (right) at a horizontal slice at z = 3000 m. The stacked energy focuses sharply at the obtained maximum of stacked energy and decays rapidly away from the maximum. The shape of the area with high stacked energy reflects the receiver geometry in a similar way as observed for the second synthetic explosion source example. In fact, it is reasonable to expect the geometrical effect to be more obvious for the location method that averages a single polarization vector because this method does not propagate any rays from pure noise back into the model.

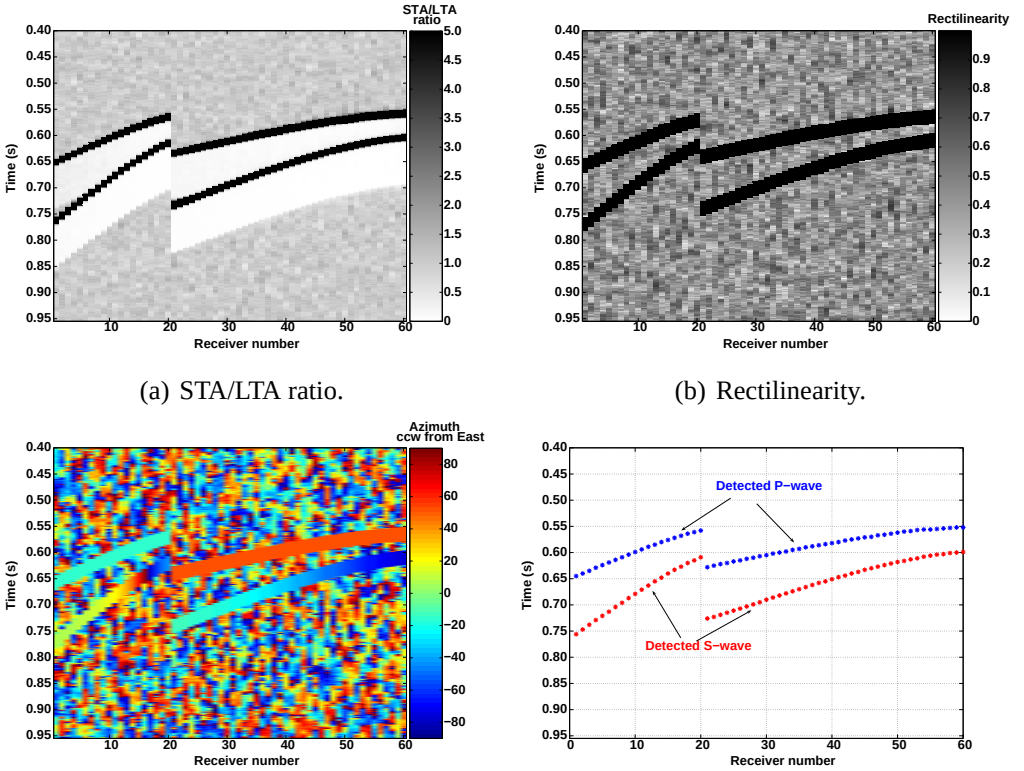

(a) STA/LTA ratio.

(b) Rectilinearity.

(c) Azimuth.

(d) Phase detection and identification.

Figure 3.13: Scheme of phase detection and identification using array-specific polarization features.

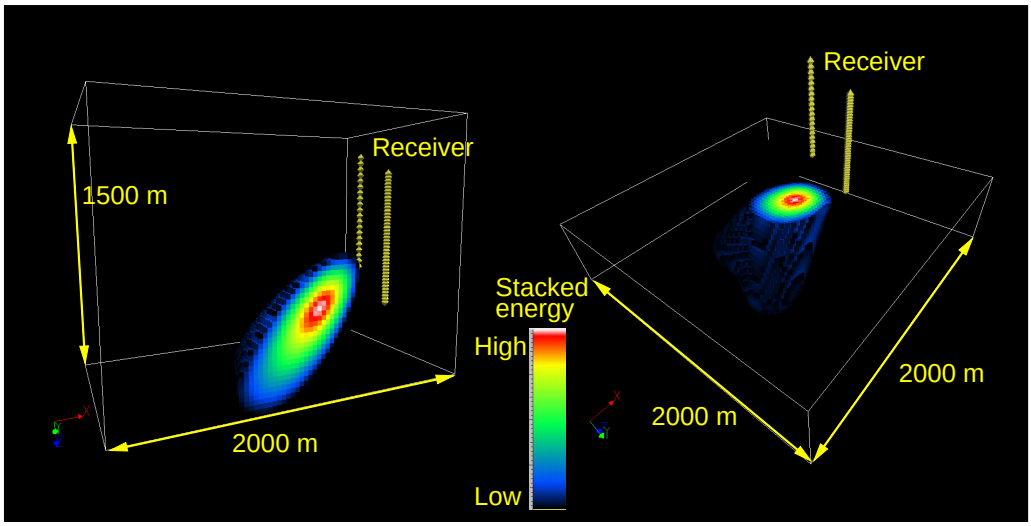

Figure 3.14: Source image obtained with the location method that uses averaged polarization information. Left: vertical slice y=100 m. Right: horizontal slice at z=3000 m. Colors represent values of stacked energy as described in Figure 3.7. The elliptical region of high stacked energy in the center of these images contains the hypocenter of the event (white spot).

3.4 Location uncertainty and signal-to-noise limits

Three examples of different receiver geometries and noise levels up to 30 % are shown in section 3.3 and for all three the maximum stacked energy corresponded to the synthetic source location. The uncertainty of location depends mainly on the signal-to-noise ratio because noise in the data affects the polarization information which is used to perform the initial-value ray tracing. Several tests on synthetic data were performed to find the signal-to-noise limit for the presented location approach. Many different synthetic data sets were computed keeping the model dimensions 2000 m x 2000 m x 2500 m and the number of receivers but varying the noise level. In order to account for different apertures the model setup was varied using three different locations of the source point; one in the center of the model (as shown in the examples for the explosion source) and two located on the edge of the model at 700 m depth and 1500 m depth, respectively. Furthermore, the receiver distribution was changed for the simulated surface stations as well as for the location and spacing of the borehole stations. The receiver spacing varied from 50 m to 100 m and the borehole was located at the edge as well as within the model. Using different noise levels, different receiver geometries and different source points about 200 different synthetic data sets were generated .

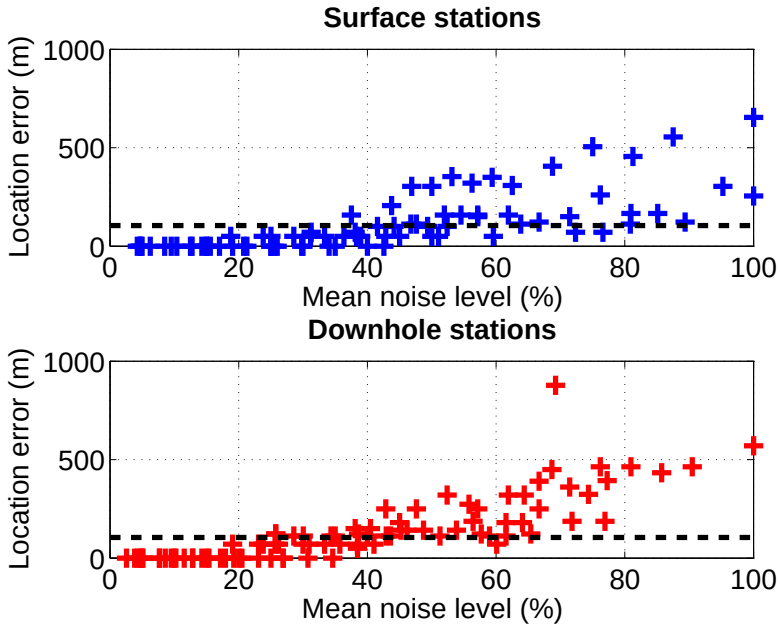

Figure 3.15: Location errors with increasing mean noise level obtained from a large number of synthetic data sets. The recording network consisted of 20 arbitrarily distributed surface stations (top) and of 20 borehole stations (bottom), respectively. The black dotted line marks the limit for locations to be considered as successful.

As described in section 2.3 the instantaneous polarization attributes are more affected by noise than the averaged polarization attributes of a time interval of a

carefully chosen length. Hence it is reasonable to assume that the location method using instantaneous polarization will be more affected by the signal-to-noise ratio. For this reason the signal to noise limits were tested using only this location method in order to estimate the lowest limit. About 50 of these data sets were located using a grid spacing of 100 m and 50 m for the other 150 data sets. For each data set the error between the obtained location and the synthetic source point was calculated. The location error at different noise levels is shown in Figure 3.15. Due to the resolution limits of the chosen grid spacing all locations with errors of less than 100 m are considered as successful locations. For arbitrarily placed receivers (Figure 3.15, top) successful locations as well as locations with no location error can be obtained for white and isotropic noise up to approximately 45 $\%$ (which corresponds to a S/N ratio of 6.9 dB)[2]. For noise levels above 45 $\%$ the majority of the estimated locations show errors larger than 100 m. Using a single linear downhole array the majority of locations show errors larger than 100 m above 35 $\%$ noise level (9.1 dB) (see Figure 3.15, bottom). For signal-to-noise ratios smaller than 6.8 dB (9.1 dB, respectively) the polarization becomes more and more disturbed in such a way that the Gaussian beams will not intersect sufficiently and hence the back-propagated energy will not clearly focus. This will be immediately visible in the final image as an increased likelihood region or as a number of small, indistinct local energy maxima. If the noise is not random (e.g., noise from a pump or tube waves in the monitoring well) then the polarization information of the microseismic signal is disturbed in a more critical way. Such a disturbance of the polarization would displace the location of the hypocenter. However, directed noise as released by pumps often has a particular frequency band and can normally be eliminated by filtering. The issue of directed noise and receiver fidelity is discussed in more detail in section 3.5. Also, perceptible discrepancies of the velocity model affect the ray tracing. Since the presented location procedures back-propagate the energy in space along rays, it is not required to calculate travel distances (as for standard location procedures) to migrate energy into the model. This makes the location accuracy more sensitive to errors in the velocity gradients (which are responsible for the ray-bending) than to errors in the absolute velocities. Thus, as long as the relative velocity contrasts are well known, the direction of the rays will not be disturbed and it will be still possible to obtain a good estimate of the true hypocenter. Furthermore, the geometry of receivers influences the shape of the likelihood region for the hypocenter as shown in section 3.3. Finally, the resolution in the image is mainly controlled by the signal wavelength as well as by the chosen grid sampling for the migration model.

[2] $SNR(dB) = 20 \cdot log_{10}\left(\frac{A_{Signal}}{A_{Noise}}\right)$

3.5 Receiver Fidelity

The most essential part in this location method is the estimation of the polarization information which defines the starting direction for the initial value raytracing. Therefore receivers with high vector-fidelity are mandatory to provide complete and accurate measurements of ground motion. One critical aspect is the receiver orientation which is necessary to interpret the ground motion vector in a 3D volume. The receiver orientation for arrays deployed at the surface can be obtained adjusting the instruments manually. In contrast, orienting receivers in a borehole is a much more delicate issue (Greenhalgh and Mason, 1995; Bland and Stewart, 1996; Zeng and McMechan, 2006). In practice, the orientation of the three component borehole geophones is beyond control of the installation crew. For this reason test shots are performed at known source locations in order to obtain the receiver orientation. The problem simplifies when the orientation of one component is fixed due to the borehole geometry. For example this is the case for receivers which are deployed in a straight vertical well. Then the vertical component can be assumed as oriented correctly. Nevertheless, the orientation of the horizontal components has to be obtained from seismic signals of known source locations. Considering a single shot and a single 3C geophone the orientation error is usually obtained in the following way. Knowing the source and assuming that the P-wave from this source propagates from the source without any lateral refraction the theoretical azimuth θ of the incoming P-wave is known (see Figure 3.16). From the seismic record of the incoming P-wave the observed azimuth τ can be estimated using hodogram analysis. The deviation between the theoretical azimuth θ and the observed azimuth τ gives the geophone disorientation $\alpha = \theta - \tau$.

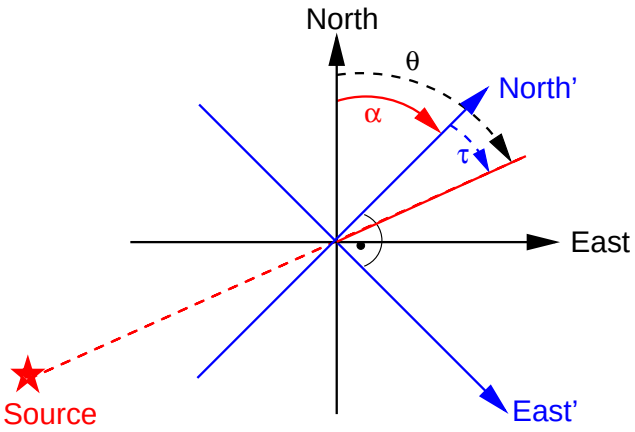

Figure 3.16: Illustration of estimating the receiver orientation.

Averaging the obtained geophone disorientation over several shots as well as analyzing relative disorientation angles on many receivers reduces the uncertainty of this estimate. Most of the commonly used methods and even the 3D orientation estimation methods are based on the polarization principle shown above.

Unfortunately, none of these methods can resolve or handle the most critical issue in receiver fidelity which is the component fidelity itself. A component fidelity can be disturbed by deviations in the geophone sensitivity or differences in the ground coupling (Drijkoningen et al., 2006) or by the presence of directed noise (De Meersman et al., 2006).

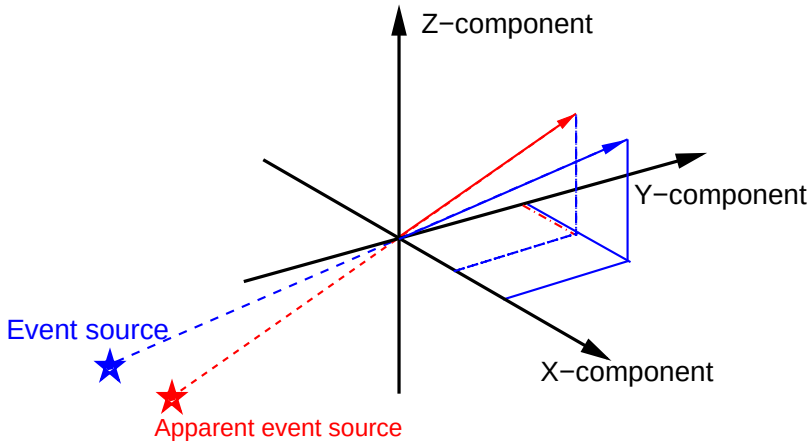

Figure 3.17: Receiver fidelity. Component values marked in blue correspond to 100 percent fidelity. The red line corresponds to 50 percent disturbed fidelity on the X-component. This disturbance results in a different vector of particle motion.

The consequences of the disturbance of component fidelity can be seen in Figure 3.17. A P-wave from the true event source (blue star) would cause the blue particle motion vector on three perfectly coupled components with equal receiver sensitivity and the absence of directed noise. If one of the components fidelity is disturbed by any of the causes mentioned before, e.g., the X-component coupling is 50 percent less than on the other components, we would observe different particle motion. Furthermore, this apparent particle motion (red vector in Figure 3.17) leads to an apparent event source (red star) or if used for the estimation of 3C receiver orientation to wrong results. For the considered example the azimuth α of the particle motion vector observed at perfectly coupled receiver components can be calculated

$$\alpha = \arctan\left(\frac{A_{H1}}{A_{H2}}\right) \tag{3.7}$$

where A_{H1} and A_{H2} denote the amplitudes recorded at the X- and Y-component of the receiver. The azimuth α' that is observed when one component is disturbed

can be calculated introducing a coupling factor for each component F_{H1}, F_{H2} and F_V

$$\alpha' = \arctan\left(\frac{A_{H1} \cdot F_{H1}}{A_{H2} \cdot F_{H2}}\right). \tag{3.8}$$

The influence of component fidelity can be estimated calculating the deviation between the true azimuth α and the apparent azimuth α'. In order to get a better impression about the disturbed fidelity-induced-errors azimuth deviations were calculated using fidelity values of 90%, 70%, 60%, 50% and 30% for the Y-component. The azimuth deviations that can be observed for a receiver with a disturbed Y-component using these fidelity values are shown in Figure 3.18. The value of deviation depends on the true emergence angle which can be explained by geometrical considerations. For example, if the incoming wave is polarized parallel to the Y-component a fidelity-disturbed X-components does not change the energy of the recorded wave nor its recorded polarization. On the other hand, if the incoming wave is polarized parallel to the X-component the disturbance on this component changes the recorded energy but not the recorded polarization. For all waves not polarized parallel to any of the component axis the energy as well as the polarization change and hence the error of the observed emergence angle depends on the true angle.

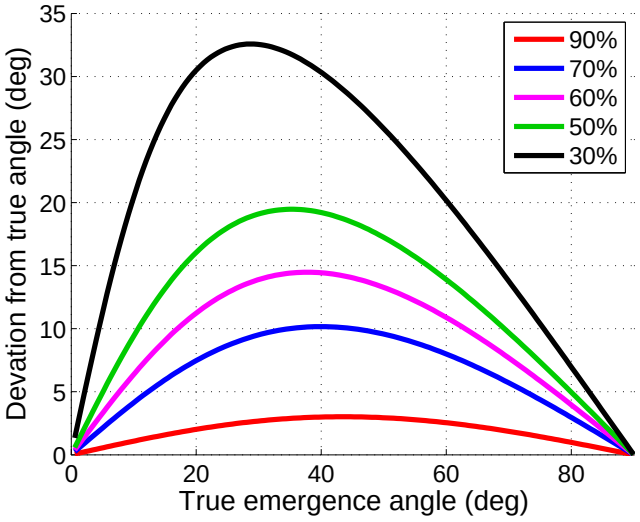

Figure 3.18: Errors in the estimation of emergence angles due to receiver fidelity disturbance. The true emergence angle is given relative to the disturbed component. The component fidelity is color coded.

Since receiver orientation estimation and component fidelity are coupled to each other either the orientation or component fidelity needs to be known to estimate the other quantity. As stated earlier in this work the developed location method

relies on polarization and hence receiver fidelity problems cannot be neglected. A solution that decouples the problem is not presented in this work.

However, in the following section a method is presented that helps to distinguish between reliable receivers and not reliable ones in order to exclude the latter from the location procedure. In the case of unknown receiver orientation test shots, perforation shots or seismic events are not suitable for component fidelity tests for the reasons mentioned above. At the same time, noise can provide useful information about the reliability of receiver components if it is random and equal from all directions. This condition is not fulfilled in the case of directed noise but this problem will be discussed later in this section. If the noise is isotropic and random from all directions a receiver perfectly coupled with equal sensitivity on all three components should show the same noise level on all three components over a sufficiently long time interval $[t_1, t_2]$. Since the noise is assumed to be isotropic the mean noise level ϖ on all three components $H1, H2$ and V is independent of the components orientation and can be obtained by:

$$\varpi_{H1} = \frac{1}{n}\sum_{t_1}^{t_2}|A_{H1}|, \qquad \varpi_{H2} = \frac{1}{n}\sum_{t_1}^{t_2}|A_{H2}|, \qquad \varpi_V = \frac{1}{n}\sum_{t_1}^{t_2}|A_V|. \quad (3.9)$$

A_{H1}, A_{H2} and A_V correspond to the amplitudes on the three components and n is the number of samples in the considered time interval. It is very important that the time interval used for this analysis does not contain any dominant polarized seismic phase arrival (e.g., from earthquakes or from test shots). These arrivals change the statistically even distributed intensity of isotropic noise. The absence of dominant phase arrivals can be automatically ensured by using STA/LTA ratios or spectrogram analysis.

Any difference in the mean noise level on the three components are caused by ground coupling problems, sensitivity problems or by the presence of directed noise. Independent of the cause it is possible to conclude that the considered receiver fidelity is disturbed. The degree of disturbance can be estimated comparing the average noise levels recorded on the different components. A normalization of the average noise levels to the component with maximum noise level even provides useful values of component fidelity F in percent:

$$F_{H1} = 100\frac{\varpi_{H1}}{max(\varpi)}, \qquad F_{H2} = 100\frac{\varpi_{H2}}{max(\varpi)}, \qquad F_V = 100\frac{\varpi_V}{max(\varpi)}. \quad (3.10)$$

Using the obtained values of component fidelity a receiver can be declared as functioning or malfunctioning. Such a decision depends on the component fidelity

values, the emergence angles of the expected waves and the desired accuracy. The influence of a malfunctioning component can be estimated as shown in Figure 3.18. Once the influence is estimated a threshold can be set in the processing procedure to exclude malfunctioning receivers from further use.

3.6 Receiver fidelity tests on synthetic data

The procedure described above was tested on synthetic data. Therefore the model setup from the last synthetic example shown in section 3.3 was utilized which consisted of 20 receivers in one monitoring well and 40 receivers in the other. For simplicity an explosion source was used to model some incoming phase arrival. Random white and isotropic noise was added to the data as described in section 3.3. Afterwards the orientation of the horizontal components was rotated also arbitrarily thereby keeping the components perpendicular to each other. Finally, a set of 180 (3×60) random numbers between 0 and 1 was generated. In order to disturb the receiver fidelity the whole synthetic trace (data and noise) of a component was multiplied by one of the random numbers. The generated traces are shown in Figure 3.19

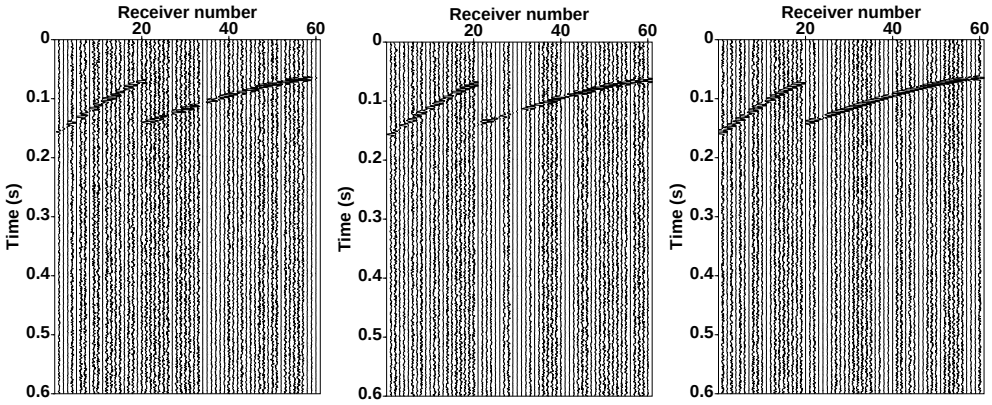

Figure 3.19: 3C synthetic data of receivers with disturbed component fidelity. From left: X-component, Y-component and Z-component.

That the component fidelity is disturbed is clearly visible at the traces. For example, receiver number 60 does not show much noise or signal on the X-component whereas the noise on the Y-component is higher and even increases on the Z-component.

The first step to analyze the receiver fidelity was to separate the noise from the incoming signal. This was achieved using the single receiver detection algorithm presented in section 3.1. Then, pure noise traces of different length were build. The aim was to test the stability of the proposed method and to estimate the optimum number of samples for such a statistical method.

In order to find a sufficient length for the noise interval (or the sufficient number of samples) time intervals of various lengths from 5 time samples to 350 time samples were build and the noise was analyzed as described above. The estimated component fidelity was compared with the random fidelity values used to disturb the receiver components. In Figure 3.20 the deviation between the true component fidelity and the estimated fidelity for different sample numbers are shown for 60 receivers. The error is color coded and increases from cool to hot colors. The colorbar was limited to 35 percent error to increase the resolution of this plot since the errors for larger time intervals are clearly below 25 percent. In other words, errors larger than or equal to 35 percent are shown in dark red. The three subfigures correspond to the different components. For all components the estimation error decreases below 25 percent when using time intervals of 100 time samples or more. The estimates of the component fidelity obtained from 100 time samples of noise at each receivers are shown in Figure 3.21. The blue curve represents the fidelity value that was used to disturb the component fidelity. The higher this fidelity value is the less disturbed was the receiver component. The red curve corresponds to the fidelity value estimated with equation (3.10). It is clearly visible that the estimated values are in a very good agreement with the true fidelity values. Even if the absolute fidelity value was not hundred percent captured by all estimates (e.g., on the x-component at receiver number 33) the overall fidelity trend can be identified using the proposed approach. Using 100 time samples of noise (as shown in Figure 3.21) already gives a sufficient estimate to decide whether a receiver has to be considered as broken or not. It is intuitive that increasing the number of time samples used for such an analysis should stabilize the estimate. An increase in the estimate stability with increasing sample number can also be seen in Figure 3.20.

Concerning a sufficient length of the investigated noise interval it is possible to conclude that the use of intervals of 50 time samples did not produce good fidelity estimates but intervals of 100 time samples did match the fidelity trend. From the numerical tests a minimum interval of 100 time samples is estimated to obtain reliable fidelity trends. The longer the noise interval the better it represents the noise conditions and the component fidelity and hence the better become the fidelity estimates.

As indicated above this method cannot distinguish whether the component fidelity is disturbed by sensitivity/coupling differences or directed noise. This means the estimated values are very useful to identify receivers where polarization analysis could be biased. On the other hand, a recalibration of the component fidelity using the estimated values is not recommended unless it is certain that the noise was random and equal from all directions and did not contain any preferred direction.

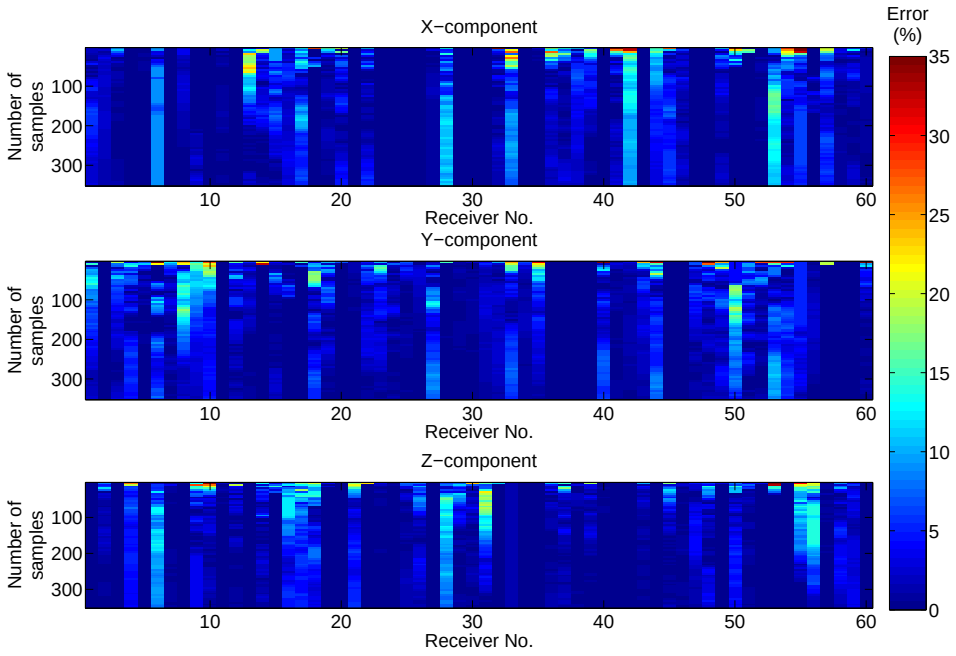

Figure 3.20: Estimation error of receiver fidelity for different number of analyzed noise samples. The error is color-coded and decreases from red to blue.

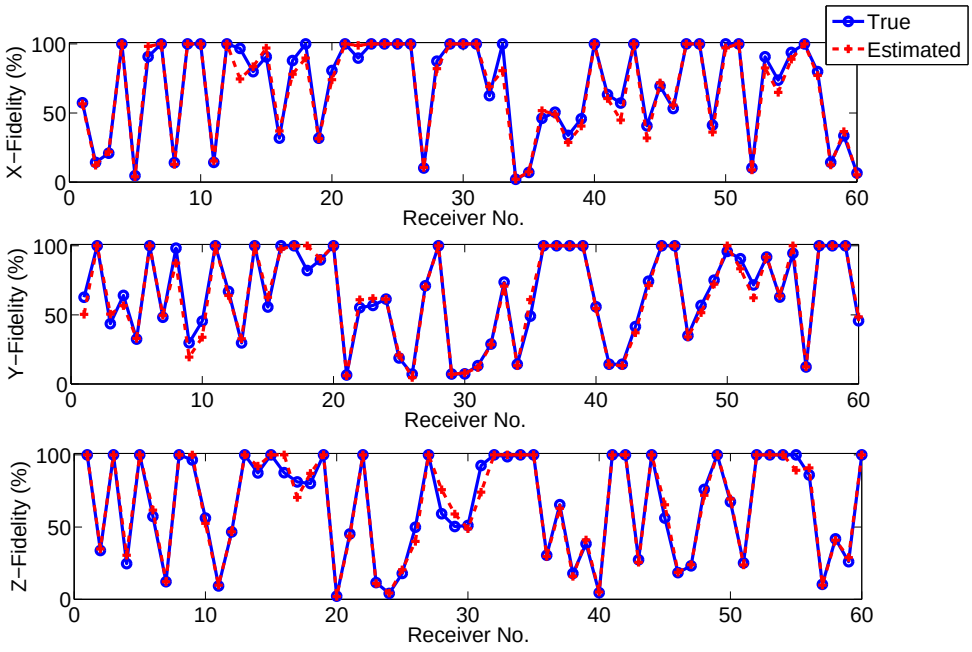

Figure 3.21: Estimation of receiver fidelity disturbance using 100 time samples of noise.